communications
earth & environment

ARTICLE

https://doi.org/10.1038/s43247-021-00188-6 OPEN

Repeating earthquakes and ground deformation reveal the structure and triggering mechanisms of the Pernicana fault, Mt. Etna

Andrea Cannata[1,2]✉, Adriana Iozzia[1]✉, Salvatore Alparone[2], Alessandro Bonforte[2], Flavio Cannavò[2], Simone Cesca[3], Stefano Gresta[1], Eleonora Rivalta[3,4] & Andrea Ursino[2]

Structure and dynamics of fault systems can be investigated using repeating earthquakes as repeatable seismic sources, alongside ground deformation measurements. Here we utilise a dataset of repeating earthquakes which occurred between 2000 and 2019 along the transtensive Pernicana fault system on the northeast flank of Mount Etna, Italy, to investigate the fault structure, as well as the triggering mechanisms of the seismicity. By grouping the repeating earthquakes into families and integrating the seismic data with GPS measurements of ground deformation, we identify four distinct portions of the fault. Each portion shows a different behaviour in terms of seismicity, repeating earthquakes and ground deformation, which we attribute to structural differences including a segmentation of the fault plane at depth. The recurrence intervals of repeating earthquake families display a low degree of regularity which suggests an episodic triggering mechanism, such as magma intrusion, rather than displacement under a constant stress.

---

[1] Università degli Studi di Catania, Dipartimento di Scienze Biologiche, Geologiche e Ambientali - Sezione di Scienze della Terra, Catania, Italy. [2] Istituto Nazionale di Geofisica e Vulcanologia, Osservatorio Etneo – Sezione di Catania, Catania, Italy. [3] GFZ German Research Centre for Geosciences Potsdam, Potsdam, Germany. [4] Università di Bologna, Dipartimento di Fisica e Astronomia, Bologna, Italy. ✉email: andrea.cannata@unict.it; adriana.iozzia@phd.unict.it

Repeating earthquakes, or repeaters, also called multiplets and earthquake families[1,2], are earthquakes characterized by the same location and fault geometry, but with different occurrence times[3]. Hence, repeating earthquakes affect the same fault area, exhibit the same slip, and share the same waveforms, provided that the medium interposed between source and seismometer has not changed[3]. Repeating earthquakes can be triggered by repeated ruptures of a fault patch driven to failure by aseismic creep on the surrounding fault plane[4,5]. They can be identified by constraining the source areas and/or analyzing the waveform characteristics[6]. Repeating earthquakes have been identified in different settings, such as plate boundary zones[4,7], active volcanoes[8,9], and glaciers[10,11].

Repeating earthquakes have many seismological applications, such as detecting temporal changes in the Earth's structure due to earthquakes[2,12] and volcanic activity[8,13] by coda wave interferometry, reconstructing the fault geometries by accurate hypocenter determinations[14–17], measuring the cumulative slip associated with the repeaters activity[4,18] and characterizing the seismic source through the empirical Green's Function approach[19].

At Mt. Etna volcano, repeating waveforms have often been observed both for long period/very long period (LP and VLP) events and volcano-tectonic (VT) earthquakes[20,21]. Concerning the VTs, most of them are shallow (focal depth <7 km b.s.l.), located in the eastern flank[22–24], and have a magnitude <2.0[23]. The VT spatial distribution is closely linked to the complex structural framework of the volcano. In fact, Mt. Etna is located on the structural domain of the Gela–Catania Foredeep, at the intersection between the front of the Apennine–Maghrebian Chain and the NNW–SSE Hyblean-Maltese Escarpment fault belt[25,26] (Fig. 1a). The eastern and southern flanks of Mt. Etna are dominated by instability, causing sliding of these volcano sectors to the east and south, respectively[27–29]. Numerous hypotheses have been proposed to explain the causes of this instability, such as increases in magma pressure in the plumbing system/magma intrusions and/or gravitational spreading and reorganization[27,30–32]. In addition, it has been suggested that flank sliding can facilitate the passive rise of magma[33].

To the north, the ~E–W-trending 18-km-long transtensive Pernicana Fault System (hereafter referred to as PF), mainly characterized by left lateral-normal motion, confines the instability of the Mt. Etna eastern flank[29] (Fig. 1a). PF extends from the NE Rift, affected by magma intrusion and formation of eruptive fissures (such as during the 2001 and 2002–2003 eruptions[34,35]), downslope to the sea[29]. PF accommodates the seaward sliding of the Etna's eastern flank with an average velocity of 1–2 cm/y[36]. PF has generated intense seismicity instrumentally recorded at least since the 1980s[37], and the earthquakes associated with its activity are mainly located in the western and central portions, while they are nearly absent in the eastern portion[38]. Depths of the foci are very shallow, mainly between the surface and about 3 km b.s.l.[38]. From 1999 to 2009, a large number of earthquake multiplets with very long repeatability over time affected the PF[21]. It is worth noting that observations of repeating earthquakes generated by PF date back to 1990[39].

While ground deformation studies have investigated the dynamics of PF[28,36,40], earthquake data have never been used to characterize the behavior of PF in terms of cumulative slip, as well as to provide insights into the segmentation of the different PF portions. Moreover, it is not clear whether the fault activity is influenced by magma pressurization in the volcano plumbing system and/or by gravitational forces. Hence, we analyzed the repeating earthquakes taking place on the north-eastern sector of Mt. Etna during 2000–2019 to shed light on these aspects. To reconcile seismic and ground deformation information, the dynamics constrained by repeating earthquake analysis has been compared with the results from the analysis of GPS data.

Results

An intense and almost continuous seismic activity occurred during 2000–2019 in the north-eastern sector of Mt. Etna (Figs. 1b, 2a, b and Supplementary Fig. 1). The number of repeating earthquake families identified was equal to 172, among which 61 PF-related families, composed of 225 events, have been extracted (Supplementary Figs. 2 and 3). The number of earthquakes making up these families ranges from 2 to 14 (36 out of 61 families are simply doublets), and the lifetime, defined as the time

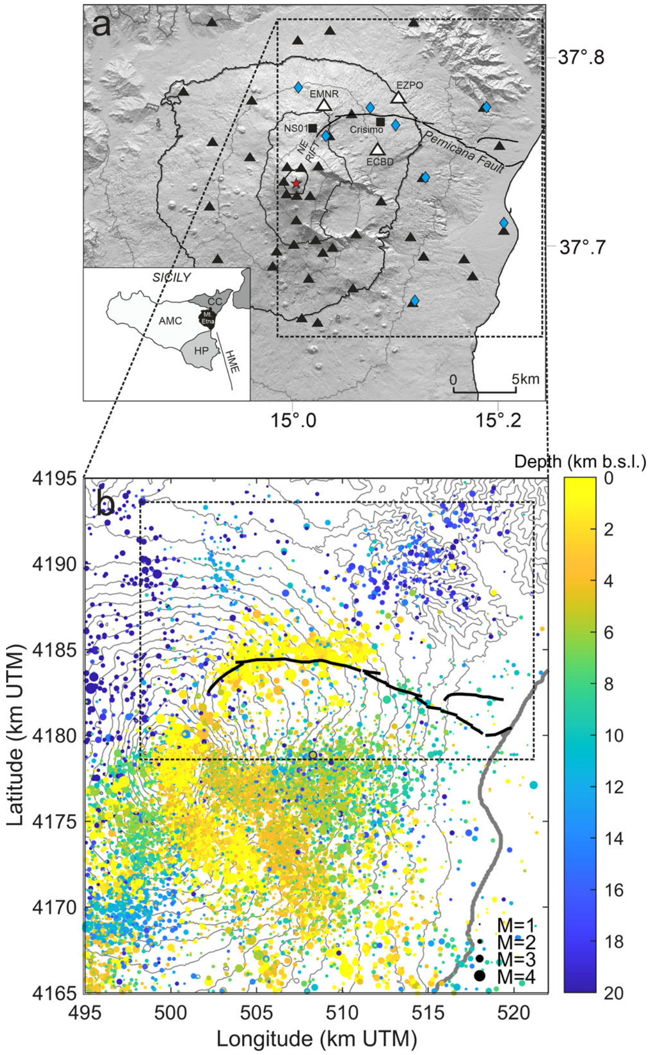

Fig. 1 Seismic and GPS networks, earthquake data. **a** Digital elevation model of Mt. Etna[74] with the locations of the seismic stations belonging to the permanent seismic network (triangles), periodic GPS stations (called NS01 and Crisimo; black squares) and permanent GPS stations (blue diamonds), run by INGV-OE and used in this work, and the Pernicana Fault (black thick line[29,61]). The white triangles indicate the seismic stations, whose signals were used to identify the repeating earthquake families (EMNR, EZPO, and ECBD). The inset in the bottom left corner of **a** shows a map of Sicily with some structural features (AMC: Apennine–Maghrebian Chain; HME: Hyblean-Maltese Escarpment; CC: Calabride Chain; HP: Hyblean Plateau[75]). The red star indicates the location of Voragine (one of the summit craters). **b** Digital elevation model of Mt. Etna[74] with the VT earthquake locations (colored dots) and the Pernicana Fault (black thick line[29, 61]). The size of the dots depends on the VT earthquake magnitude (see black dots in the lower right corner) and the color on the focal depth (see the colorbar). The dashed rectangle in **b** indicates the area investigated in this work.

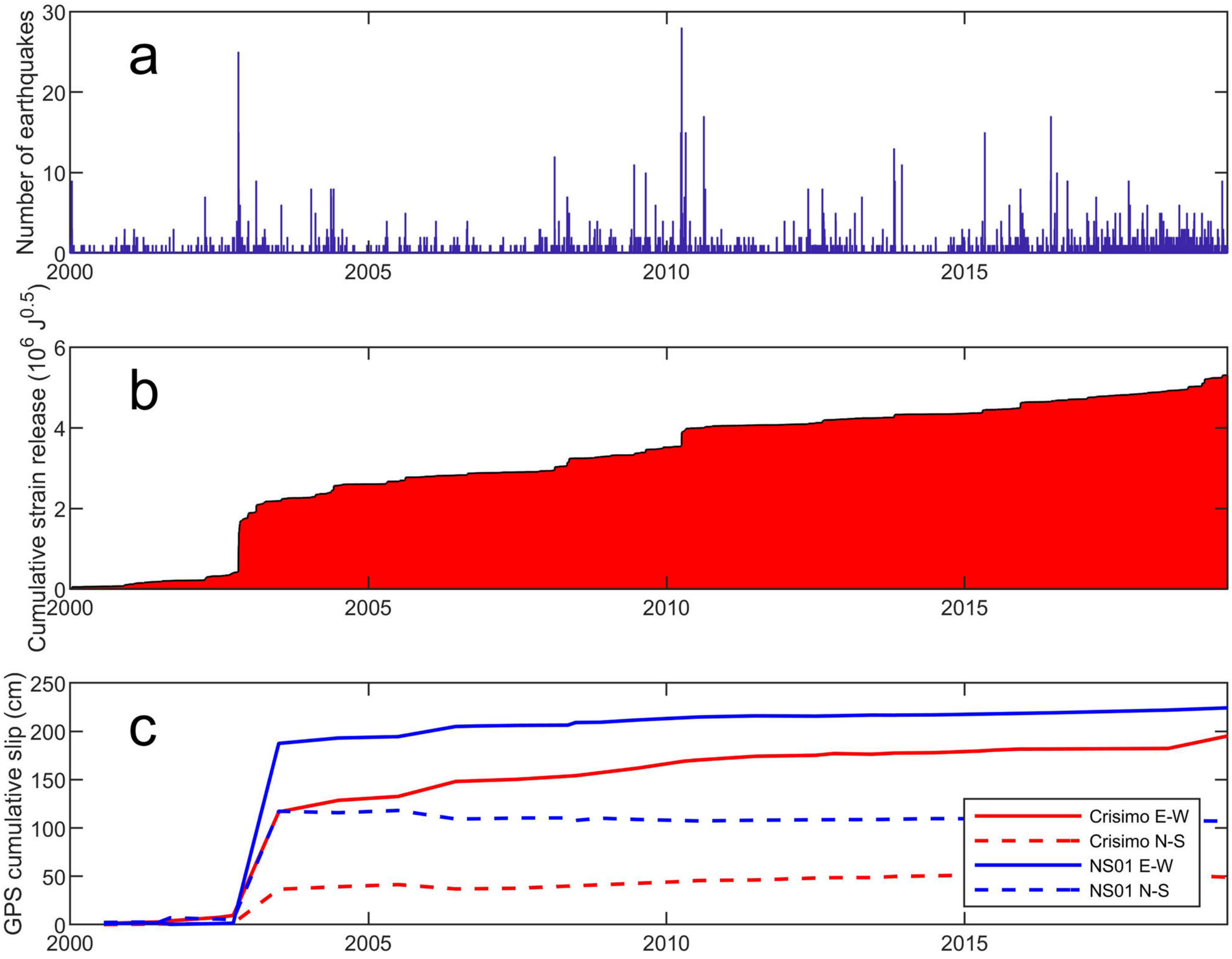

Fig. 2 Time series of seismicity and ground deformation during 2000–2019. a Histogram showing the daily number of the earthquakes located within the north-eastern sector of Mt. Etna (see dashed rectangle in Fig. 1b). **b** Area plot showing the cumulative strain release of the earthquakes in (**a**). **c** Cumulative displacement measured by Crisimo and NS01 stations, belonging to the periodic GPS network.

between the first and the last earthquakes in a family, ranges from less than 1 h to the duration of the entire analyzed catalog, that is almost 20 years (Figs. 3a, c and 4a, b). On the basis of the definitions given by Igarashi et al.[41], most of the PF families (47 out of 61) are "*nonburst-type*", with a lifetime longer than 3 years.

In addition, we calculated the coefficient of variation (hereafter referred to as COV), defined as the standard deviation divided by the mean and showing the probabilistic behavior of a random variable, to quantify the variability within the repeating earthquake families[4]. The COV computed on magnitude shows low values, ranging between 0.1 and 0.4, suggesting relatively constant magnitude values within each family (Fig. 4c). On the other hand, the COV computed on inter-event times (defined as the time span between successive events) shows higher values of ~0.6–1.3 (Fig. 4d), as well as a wider range suggestive of a broad variability in the occurrence behavior of the earthquakes belonging to the families. COV values close to 0 indicate periodicity or quasi-periodicity, COV equal to 1 Poissonian recurrence, and COV greater than 1 temporal clustering (e.g., ref. [42]). It is worth noting that we did not calculate COV on inter-event times in case of doublets. We ruled out the possibility of "artificially high" COV values for small inter-event times by examining the relationship between COV computed on inter-event times and the mean inter-event times values (Supplementary Fig. 4).

Repeating earthquake analysis allowed identifying four PF portions with different features (Fig. 3), called eastern portion (longitude comprised between 512 and 520 km UTM; hereafter referred to as EP), central portion (longitude 508–512 km UTM; CP), western portion (longitude 503–508 km UTM; WP1) and westernmost end of the fault (longitude 501–503 km UTM; WP2). All the repeating earthquake families are located along CP, WP1, and WP2 (Fig. 3), while EP exhibits no repeating earthquakes at all. This was expected, as the area where the eastern portion of the PF is located appears to be almost unaffected by shallow (focal depth <5 km b.s.l.) seismicity, which characterizes the CP, WP1 and WP2 (Fig. 1b). Regarding the temporal distribution of the PF repeating earthquakes, there are three main periods characterized by intense activity (Supplementary Fig. 5): (i) during and after the dike intrusion that led to the Mt. Etna 2002–2003 eruption, when mostly WP1 and CP gave rise to repeating earthquakes; (ii) in April 2010, when a seismic swarm affected WP2, WP1, and CP; (iii) in December 2015, a few days after the lava fountain sequences at Voragine (one of the Mt. Etna summit craters; see Fig. 1a), when mainly WP2 and WP1 generated repeating earthquakes.

We divided the time series of cumulative slips of each PF-related family (calculated by Eq. 2) into groups according to the longitude of the family centroid (Supplementary Fig. 6). Successively, per each 1-km-long longitude range, we selected the family with the highest value of total cumulative slip during the analyzed period (Fig. 5b and Supplementary Fig. 6). The part of the PF

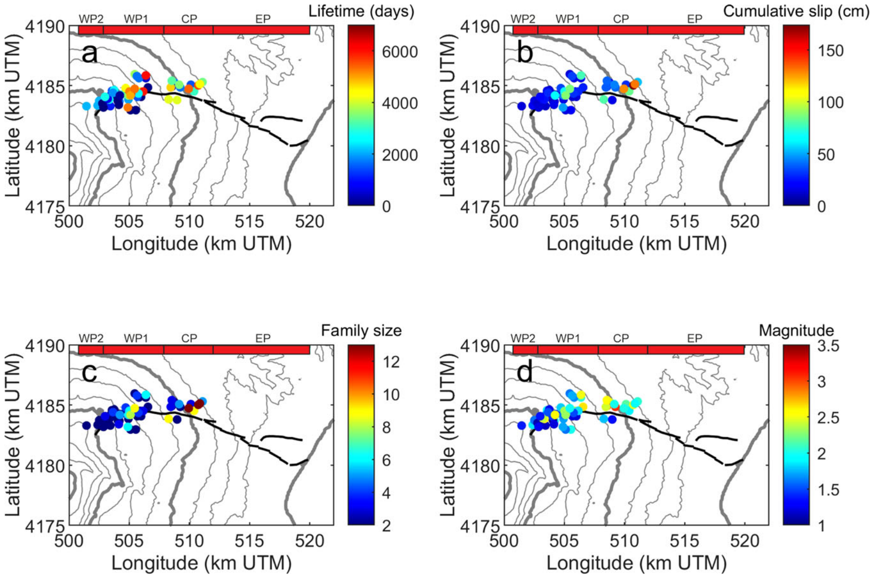

Fig. 3 Spatial variation of the features of the PF repeating earthquake families. Digital elevation model of Mt. Etna north-eastern sector[74] with PF (thick black line) and locations of the centroids of the repeating earthquake families located along PF (colored dots). The color of the dots indicates family lifetime (**a**), cumulative slip calculated per each family (**b**), number of earthquakes composing each family (**c**) and the average magnitude of each family (**d**). The red bar at the top of each plot shows the portions of PF, characterized by different features. EP eastern portion, CP central portion, WP1 western portion, WP2 westernmost portion.

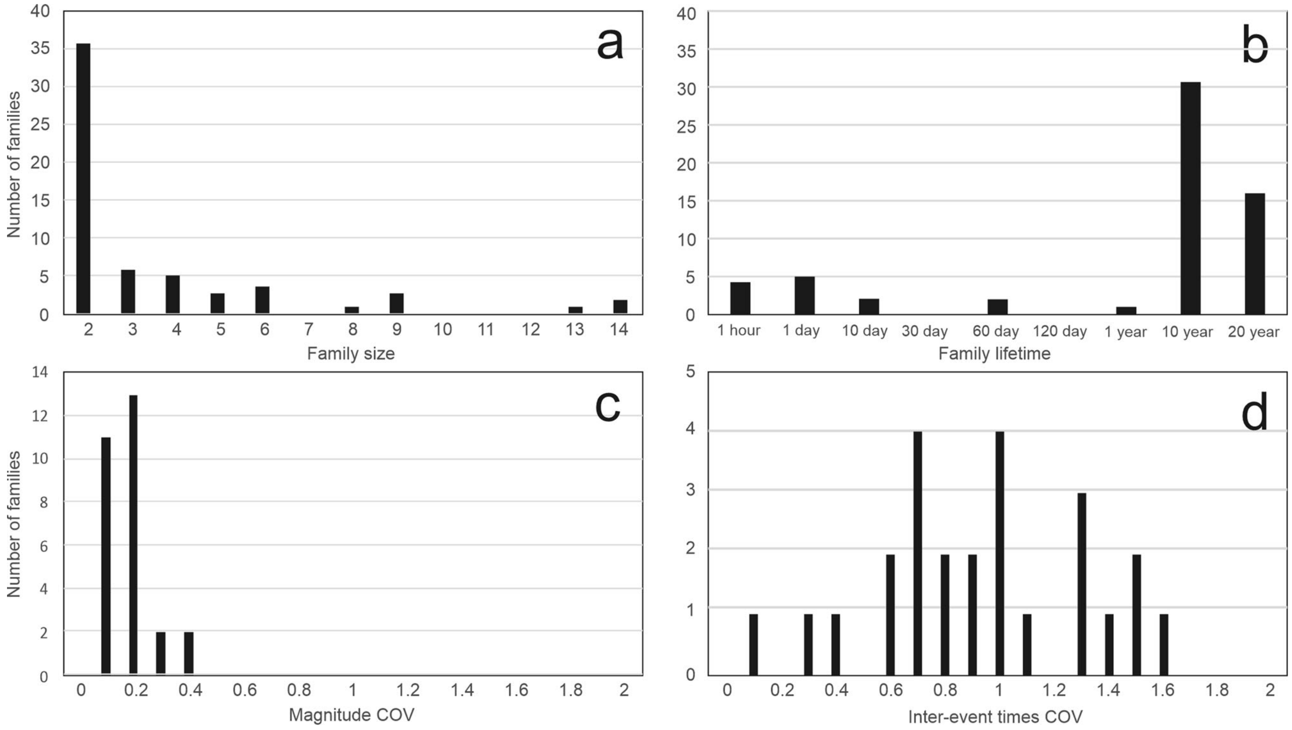

Fig. 4 Main features of the PF repeating earthquake families. Histogram showing the number of families located along PF with a given number of earthquakes (**a**), lifetime (**b**), COV computed on magnitude (**c**) and COV computed on inter-event times (**d**).

with the maximum cumulative slip (~130–180 cm at longitude of 509–511 km UTM) is the CP, while the WP2 shows much lower cumulative slip, ranging from ~15 to ~20 cm (Fig. 5). Moreover, CP is also characterized by the most populous families and the highest magnitude values (Fig. 3c, d). On the other hand, it must be noted that WP1 (at longitude of 503–506 km UTM) shows a much higher number of earthquake families (12–19) compared to CP (6) (Supplementary Fig. 6).

Changes over longitude of the cumulative strain release, the maximum cumulative slip by repeating earthquakes and the GPS ground deformation data were plotted in Fig. 6 to show the spatial variability of the PF. In particular, we estimated the first parameter by considering all the earthquakes of the catalog (not just the repeating earthquakes) falling within 2-km distance from the PF and grouped into 1-km-long longitude intervals, as well as only the PF repeating earthquakes. We computed the second one as the maximum

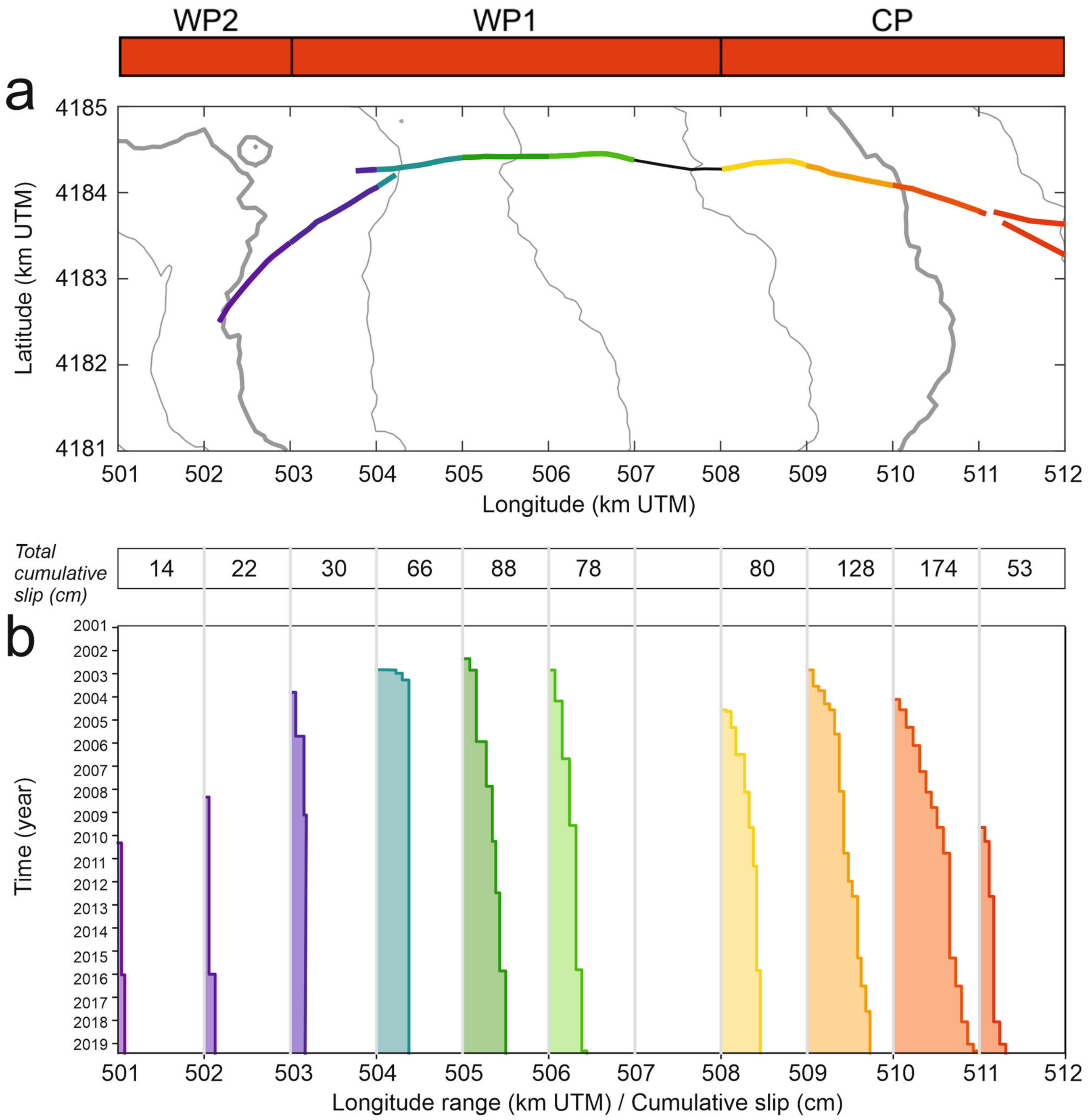

Fig. 5 Slip histories of the main PF repeating earthquake families. a Digital elevation model of the north-eastern sector of Mt. Etna[74] showing the PF (colored line). The color of the segments of PF are the same as the stairs plot in (**b**). **b** Stairs plots showing the cumulative slip histories of repeating earthquake families. In particular, only the families showing the maximum total cumulative slip, in each 1-km-long longitude range, are shown. The total cumulative slip of each time series is shown at the top of (**b**). The red bar at the top of **a** shows three of the four portions of PF, characterized by different features. CP central portion, WP1 western portion, WP2 westernmost portion.

cumulative slip calculated based on the repeating earthquake families again grouped into 1-km-long longitude intervals (Fig. 5b and the thick black line in Supplementary Fig. 6). Concerning the GPS results, the stations Crisimo and NS01, belonging to the GPS periodic network, provided East-West displacement data for the whole analyzed period 2000–2019 (Fig. 2c). In addition, the GPS permanent network supplied information only for the most recent time span (2012–2019) but with higher spatial resolution, that allowed constraining both slip and opening variations along PF, modeled as composed of four linear segments (Fig. 7a, b).

Regarding the time-related families, we found 47 temporal links among the families (see examples in Fig. 8). It is worth noting that, although the maximum temporal difference among the events was fixed to 5 days, the median lag value calculated among the detected pairs of close events in time is 1.3 days. Moreover, the median distance among the centroids of the time-related families is 1.7 km. Hence, the events belonging to such time-related families tend to occur closely in space and time, suggesting how the mechanism temporally linking the different families is quick and effective especially at very close distances.

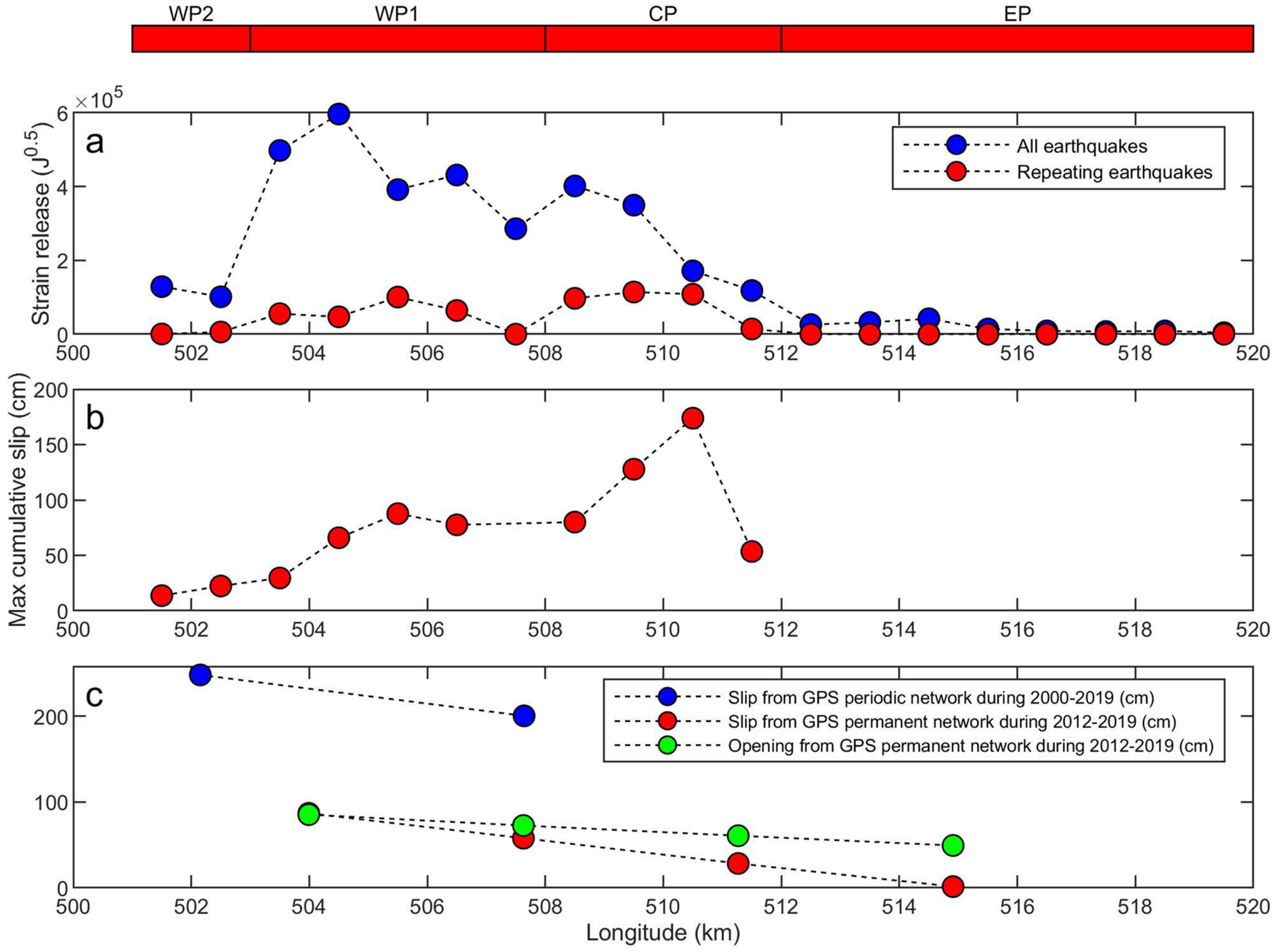

Fig. 6 Variation of the main features of PF along the longitude. Variation of seismic strain release (**a**), maximum cumulative slip constrained by repeating earthquakes (**b**) and cumulative displacement measured during 2000–2019 by two stations of the periodic GPS network (Crisimo, longitude 507.6 km UTM; NS01, longitude 502.2 km UTM), and slip and opening along the PF during 2012–2019 constrained by data from GPS permanent stations (**c**). The red bar at the top of **a** shows the portions of PF, characterized by different features. EP eastern portion, CP central portion, WP1 western portion, WP2 westernmost portion.

Discussion

We found numerous repeating earthquakes at PF, which have allowed us to investigate its dynamics. It is possible to divide the whole length of PF into four portions, characterized by different behaviors in terms of VT seismicity and more specifically of repeating earthquakes, which reflect important structural differences.

Moving from East to West, EP not only lacks any family of repeating earthquakes (Fig. 3), but it is almost completely devoid of any shallow seismicity (Figs. 1b and 6a; highlighted also by previous studies, e.g., refs. [23,38]) and is characterized by both minimum slip and opening as measured by the GPS permanent network (Fig. 7a, b). Such a PF portion appears as a complex shear system made up of en échelon left-lateral faults[29], whose location is suggested by surface evidence and damage caused to edifices by creep phenomena[29,34,43].

Conversely, CP is characterized by intense seismicity (Fig. 1b) and a few families with the highest number of events and magnitude, as well as with the highest corresponding cumulative slip (up to 174 cm at longitude 510–511 km UTM; Figs. 3, 5, 6b). This repeating earthquake-derived slip roughly matches the slip measured by the E–W component of Crisimo GPS station during the entire period analyzed (~200 cm; Fig. 2c). In addition, CP is also characterized by higher slip values as constrained by permanent GPS data during 2012–2019 than EP (Fig. 7a). It is also worth noting that for one segment of such a fault portion (longitude 510–511 km UTM) the cumulative strain release, computed by only repeating earthquakes, is similar to the cumulative strain release by the whole seismicity in the area (Fig. 6a), suggesting that most of the earthquakes taking place in this fault part are multiplets. From the structural point of view, CP shows a sinistral slip with an individual N110° trending steep fault escarpment[29]. All these features suggest that PF is here characterized in depth by a single fault plane with asperities working as creep gauges, allowing to measure the fault slip.

Moving westward (WP1), we find the portion of PF with the highest strain release (Fig. 6a) and the highest number of repeating earthquake families (up to 19 families at longitude of ~503–504 km UTM; Supplementary Fig. 6). Each of these families is generally composed of fewer events and smaller magnitude compared to the families in CP (Fig. 3). Hence, unlike the highest slip values constrained by GPS data (Fig. 7a), the cumulative slip computed by repeating earthquakes in WP1 is lower (~30–90 cm) than the one computed for CP (Fig. 5), as well as than the one measured by NS01 GPS station (~220 cm; Fig. 2c). On the surface, WP1 appears as an ENE-WSW trending fault defined by a set of extensional fractures, directly, structurally, and kinematically connected to the NE Rift[29,44,45]. All these features are likely to be suggestive of a segmentation of the fault plane in depth. Thus, each fault segment, exhibiting asperities and then giving

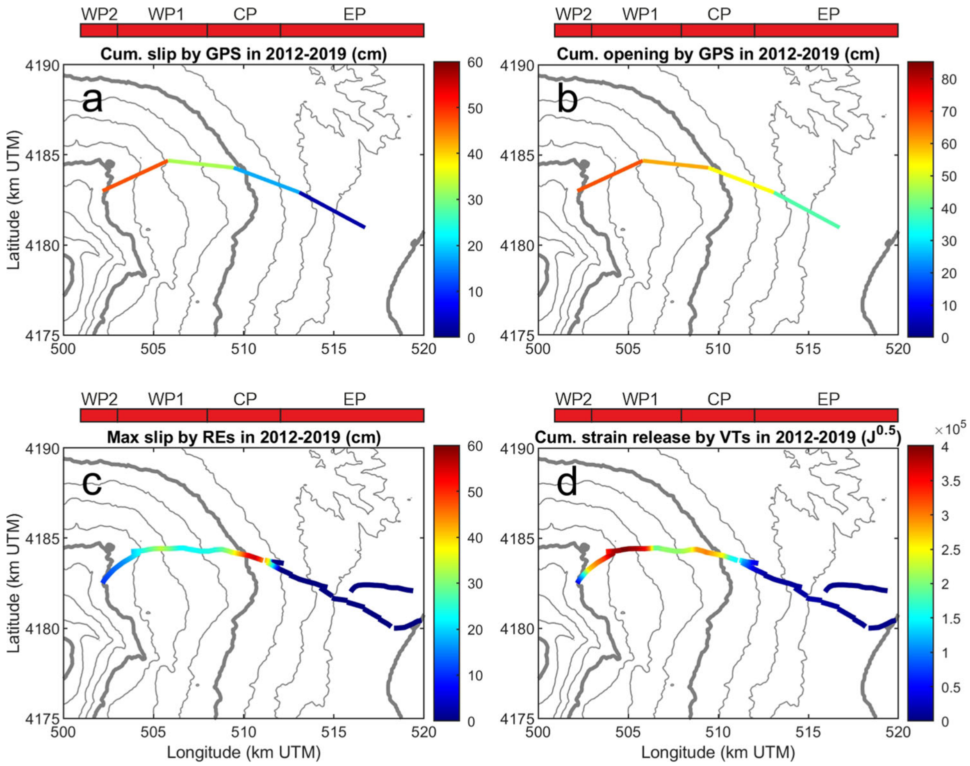

Fig. 7 Kinematic features of PF during 2012–2019, constrained by repeating earthquake and GPS data. Digital elevation model of the eastern sector of Mt. Etna[74] showing the PF (colored line) with information concerning the period 2012–2019. The color depends on the cumulative slip constrained by GPS permanent network (**a**), on the cumulative opening constrained by GPS permanent network (**b**), on the maximum cumulative slip estimated by repeating earthquakes (**c**), on the cumulative strain release estimated by VT earthquakes (**d**). In **a**, **b** the PF is modeled as composed of 4 linear segments. The red bar at the top of each plot shows the portions of PF, characterized by different features. EP eastern portion, CP central portion, WP1 western portion, WP2 westernmost portion.

rise to repeating earthquake families, probably accommodates only part of the total fault slip. It is worth noting how most of the strongest earthquakes occurring on PF (with magnitude ranging from 3.6 to 4.3) take place along WP1 and CP at longitude ranging from 503 to 510 km UTM, characterized by most of the detected repeating earthquake families (50 out of 61; Supplementary Fig. 7).

Finally, the westernmost end of the fault (WP2) is characterized by a decrease in the VT seismicity (Figs. 1b and 6a) and by a few families (1–5) with a few events (2–3) composing each family, as well as by the lowest cumulative slip (Figs. 3, 5 and Supplementary Fig. 6). WP2 is connected to the NE Rift, and has been affected in the past by magma intrusions and formation of eruptive fissures[34,35]. This is also confirmed by the highest opening values, reached in this PF sector, constrained by data from the permanent GPS network (Fig. 7b). For this reason, this PF sector is probably not capable of effectively generating many repeating earthquakes, as well as more generally VT seismicity. It is also worth noting that the earthquakes taking place in WP2 show low magnitude (mostly lower than 2; Fig. 3d). Hence, we cannot exclude that some events generated by this fault sector have been neglected, especially during the first part of the analyzed time interval, when one-component short-period seismometers were used to monitor Mt. Etna seismicity.

Important differences among the portions of PF also concern the shape of the slip histories, as shown in Fig. 5 and Supplementary Fig. 6. Indeed, while WP1 and WP2 show slips temporally concentrated in particular time spans, CP is characterized by slips spread over almost the entire period analyzed.

Moving from a spatial to temporal analysis, three periods showed intense repeating earthquake activity along PF (Supplementary Fig. 5), two of which (during and after the dike intrusion leading to the 2002–2003 eruption and a few days after the 2015 lava fountains at Voragine crater) are associated both with eruptions and with activities in the magmatic system[34,46], while the third one (April 2010) is related to the tectonic loading due to the sliding of the eastern flank[47]. Hence, also the repeating earthquakes suggest how different phenomena can affect the PF activity, first of all magma intrusion/pressurization of the volcano plumbing system and gravitational forces[27,30–32]. It is also worth pointing out that 11 out of the 13 strong earthquakes with $M > 3.5$ took place during these three time periods, suggesting that the link between intense seismicity and repeating earthquakes is not only spatial but also temporal.

In this respect, the recurrence behavior of the events belonging to the PF earthquake families can provide further evidence. Indeed, COV values, ranging from ~0.6 to 1.3, indicate variable inter-event times and lack of periodicity, and hence a low degree of regularity (Fig. 4d). Thus, it is possible to infer that such events do not derive from a constant stressing rate acting on the asperities, as obtained in some tectonic areas along plate boundaries, where inter-event time COV values are much lower than 1[42,48]. The observed variability in the inter-event times can be due to the interactions of PF with other faults by static stress transfer or even by dynamic stresses, in case of remote triggering from distant earthquakes[49–51]. In addition, the occurrence times of the events belonging to the families are influenced by the role played by PF in accommodating the seaward sliding of the Etna's eastern flank, which as aforementioned is mainly driven by intrusion/pressurization of the volcano plumbing system and gravitational forces. Focusing on the westernmost part of the PF connected to the NE Rift (WP2), intrusions and/or pressurization phenomena of the central plumbing system could directly affect the occurrence

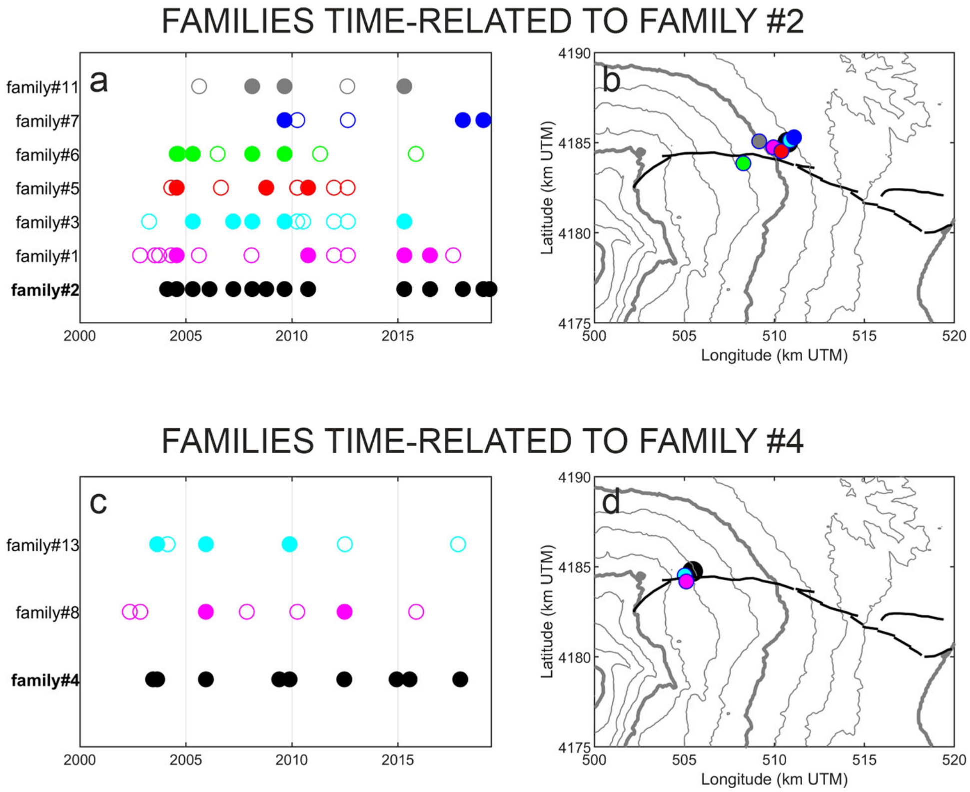

Fig. 8 Repeating earthquake families time-related to each other. Examples of families time-related to family #2 (**a**, **b**) and #4 (**c**, **d**), chosen as reference families. **a**, **c** Time distribution of the events belonging to the repeating earthquake families time-related to family #2 and #4, respectively. The black dots represent the events belonging to the reference family, the colored dots the events belonging to the families time-related to the reference family (the colored solid dots indicate the events with a time difference lower than 5 days with the events belonging to the reference family). **b**, **d** Digital elevation model of the north-eastern sector of Mt. Etna[74] with the PF (black thick line) and locations of the centroids of the repeating earthquake families shown in (**a**, **c**), respectively.

times of the events. We also calculated the median value of the inter-event time COV per each portion of the fault, except for EP which does not show any repeating earthquake family. WP2 has only one family with more than 2 events and then we calculated only one COV value equal to 1.41, while WP1 and CP showed 0.93 and 0.75, respectively. Hence, no evident differences among the PF portions were found.

We also highlighted temporal links among families (Fig. 8). In particular, the mechanism linking the different families turned out to be quick and effective especially at very close distances, as testified by median lag and distance, among the detected linked pairs of events, equal to 1.3 days and 1.7 km, respectively. As suggested by Chen et al.[49] who analyzed the repeating earthquake sequences in the Parkfield region (California), such temporal relationships among families can be due to: i) common triggering by a local slow-slip transient spanning the clusters, or ii) short-term triggering between very close-by events. GPS data show a clear acceleration in the cumulative slip during the 2002–2003 eruption (Fig. 2c), and hence the detected pairs of close events in time belonging to the different families, taking place during this period, are likely to result from the acceleration in the eastern flank sliding triggered by the magma intrusion (hence a phenomenon similar to "i"). On the other hand, other event pairs did not occur during periods with evident acceleration in cumulative slip as measured by GPS data, suggesting that the phenomenon (ii) can be also relevant.

Conclusions. The analysis of the catalog of VT earthquakes occurring in the north-eastern flank of Mt. Etna during 2000–2019 allowed us to identify an extraordinary wealth of families of repeating earthquakes generated by the PF, an ~E–W-trending 18-km-long transtensive structure accommodating the seaward sliding of the volcano's eastern flank.

We identified four portions of PF, characterized by different features of the repeating earthquake families. The eastern portion of PF (EP), whose location is only suggested by surface evidence and damage caused to edifices by creep phenomena, does not show any family of repeating earthquakes. The central portion (CP) shows few very populous families, whose corresponding cumulative slip roughly matches the slip measured by GPS stations, suggesting how here the repeating earthquakes work as effective creep gauges allowing to measure the fault slip. On the other hand, the western portion of PF (WP1) exhibits numerous families with a low number of events and then a much smaller cumulative slip compared to the slip measured by GPS stations. This likely results from a segmentation of the fault plane in depth; each fault segment, exhibiting asperities and then giving rise to certain repeating earthquake families, accommodates only part of the total fault slip. Finally, the westernmost tip of PF (WP2), connected to the NE Rift and affected by magma intrusions, is largely aseismic and characterized only by a few families with low repeatability.

The events belonging to the PF earthquake families lack periodicity and show a low degree of regularity. This suggests that the earthquakes composing the families do not derive from a constant stressing rate acting on the asperities, but rather from episodic triggering phenomena, linked to the role played by PF in accommodating the seaward sliding of the Etna's eastern flank. Such a sliding can be triggered by both magma intrusion/pressurization of the volcano plumbing system and gravitational forces.

Furthermore, temporal links among repeating earthquake families have been identified. The mechanism behind such links turned out to be quick and effective especially at very close distances, and hence it consists of (i) common triggering by the acceleration phenomenon in the eastern flank sliding, and (ii) short-term triggering between very close-by events.

Finally, our study shows how the integration of repeating earthquakes and ground deformation data can help investigate the dynamics of a fault in detail, even in a complex volcanic system as Mt. Etna, dominated by a complicated interplay of eruptive and tectonic phenomena. The same approach could be extended to other faults characterized by repeating earthquake activity, to provide insights into their behavior and its changes over time.

Methods

Data. The dataset comprises 1863 VT earthquakes (hereafter simply referred to as earthquakes) with magnitude from 0.5 to 4.3 (average and median magnitude values are equal to 1.6 and 1.5, respectively), located in the north-eastern sector of Mt. Etna and recorded from 1 January 2000 to 31 May 2019 by the permanent seismic network managed by the Istituto Nazionale di Geofisica e Vulcanologia-Osservatorio Etneo (INGV-OE) (Fig. 1b and Supplementary Fig. 1[52–54]). The earthquakes were located using the Hypoellipse algorithm[55] and a 1D crustal velocity model, proposed for Mt. Etna by Hirn et al.[56] and subsequently modified by Patanè et al.[57]. In particular, the top of the crustal velocity model is set at 1600 m a.s.l and the altitude of the seismic stations was taken into account.

The temporal distribution of these earthquakes, as well as their cumulative seismic strain release, are plotted in Fig. 2a, b. The strain release of each earthquake was calculated as the root square of the energy, calculated by using the equation:[58]

$$\log(E) = 9.9 + 1.9M - 0.024M^2 \quad (1)$$

where E is the energy in erg and M the local magnitude.

To perform the cross-correlation analysis, we used three seismic stations located on the north-eastern sector of Mt. Etna: EMNR, EZPO, ECBD (Fig. 1a). During the 20 years analyzed, the quality of the sensors equipping these stations improved over time, from analog, one-component, short period (1 s) to digital, three-component, broadband (40 s) seismometers. We selected these three stations because of their locations, very close to the PF, the long-time recording period, and the good signal to noise ratio.

Repeating earthquake detection. We band-pass filtered the signals between 1 and 20 Hz by a Butterworth 2-pole filter. The high-pass filter at 1 Hz was applied to minimize the possible waveform differences at the lower frequency end due to the distinct sensors (short-period and broad-band) installed during the considered 20 years. The low-pass filter at 20 Hz was implemented to reduce the anthropogenic high frequency noise. Once the signals were filtered, 5-second-long signal windows, starting 0.5 s before the *P*-wave arrival time, were extracted from the vertical component of the seismic signals recorded by the three stations. Due to the short distance between seismic sources and stations, 5-second-long windows comprise both P- and S-phases. Successively, we computed a cross-correlation matrix for each station, populated by the cross-correlation coefficients obtained by comparing the waveforms of earthquake pairs recorded at the same station.

We applied the following method to extract the repeating earthquake families from each cross-correlation matrix[59] (see Supplementary Fig. 2 for a schematic example of the repeating earthquake detection method). The earthquake with the highest number of correlation values above the threshold (0.9, as also reported below) was identified, and all the events well-correlated with it were stacked to find an average family waveform. This stacked waveform was again cross correlated with the original seismic record. All the earthquakes with a correlation greater than the threshold were grouped into a family and removed from the matrix. The same process was applied on the remainder matrix, until the entire matrix was organized into distinct families. Unlike the "*bridging technique*"[60], the algorithm described guarantees that all the earthquakes belonging to a family are "similar" to a single waveform, namely the stacked one. A cross-correlation threshold equal to 0.9 was chosen to extract the families. Finally, we merged the results obtained by the three stations:[21] if the earthquake "a" belongs to the family "1" at the station "STA1" and to the family "2" at the station "STA2", the families "1" and "2" are unified into a single family. Examples of waveforms of the repeating earthquakes belonging to a family (named #3) and recorded by all the three used stations are shown in Supplementary Fig. 3.

Successively, to extract the families related to the PF activity, firstly the centroid location of each family was computed as the point having the average coordinates among the earthquakes belonging to the family. Then, the families whose centroid is located at a maximum horizontal distance of 2 km from the PF line (as indicated by the literature; e.g., ref. [29,61]) shallower than 5 km b.s.l. were considered as related to the PF activity (Fig. 3). The horizontal distance threshold of 2 km was chosen based on the location horizontal errors of the earthquakes, particularly high (up to 3 km) in the first part of the catalog (2000 - 2003). In addition, such a threshold should account for possible deviations from a perfect vertical dip of the fault in depth. On the other hand, the 5 km depth threshold is typical for the PF seismicity, as suggested by previous studies[38,62].

Once the repeating earthquakes related to PF were identified, Supplementary Fig. 5 was drawn to visualize their time-space variability, showing the longitude—time distribution of all the repeating earthquakes belonging to the PF families.

Slip computation. We calculated the slip of each repeating earthquake with the equation:[42]

$$d = 10^{-2.36} {M_0}^{0.17} \quad (2)$$

where d is the slip in cm and M_0 the seismic moment in dyne cm. Successively, we calculated the cumulative slip of each family by summing the slip values obtained for all the repeating earthquakes belonging to the family. The Eq. (2) derives from the analysis of 53 sequences of small-magnitude repeating earthquakes in the Parkfield region (California), which took place from 1987 to 1996[42]. This equation was then applied to repeating earthquakes in other areas (e.g., eastern Taiwan[63]; north-eastern Japan[64]; south-western Japan[7]). We computed the seismic moment M_0 from the local magnitude values (M_L) as follows:[65]

$$\log(M_0) = (17.60 \pm 0.37) + (1.12 \pm 0.10)M_L \quad (3)$$

Families time-related to each other. Following the work by Chen et al.[49], we sought evidence of possible temporal "links" among the different PF families to understand whether the earthquake families interact with each other in a way that is observable in the relative occurrence times. In particular, we investigated the temporal relationships among the events belonging to the PF families: (i) a given family was taken into account as the reference family; (ii) the temporal differences between the occurrence times of all the events belonging to the reference family and the occurrence times of all the other events not belonging to the reference family were calculated; (iii) all the families showing at least three events with a time difference shorter than 5 days with the events of the reference family were considered "time-related" to the reference family. These steps were repeated as many times as the number of PF families, each time considering a different family as reference.

Ground deformation data. To study the ground deformation taking place in the PF area, we used GPS stations belonging to both GPS permanent[66] and GPS periodic[67] networks, managed by INGV-OE. The permanent network performs a continuous monitoring of the ground deformation, while the periodic network consists of geodetic benchmarks measured by GPS in survey mode at least yearly, to increase the spatial details needed for imaging the complex ground deformation pattern of Mt. Etna volcano.

We used Crisimo and NS01 stations belonging to the NE sector of the GPS periodic network (Fig. 1a). These stations, used to monitor the deformation related to the PF especially during seismic and volcanic crises[68,69], provided ground deformation data for the whole time interval (2000–2019). In particular, we considered the displacement along the East-West direction, reflecting the slip along the PF (Fig. 2c).

In addition, we used eight GPS stations, spatially distributed on both sides of the PF, belonging to the GPS permanent network to estimate the slip distribution along the fault from ground deformation data (see blue diamond markers in Fig. 1a). We processed the raw GPS observations using the GAMIT/GLOBK software[70] to produce time series of daily station positions. To ensure consistency in the results, we processed the longest available period in which all stations were regularly functioning (2012–2019).

To restrict the analysis to the differential deformation due only to the fault kinematics, thus avoiding the definition of an outer reference system, we considered the relative displacements measured along baselines. The baseline variations were calculated from the position time series for all the pairs of stations whose link crosses the fault. We used cumulated baseline horizontal variations in the considered period to estimate the kinematic parameters along the PF. To this end, the PF was divided into 4 segments and the predicted deformation field at the surface was calculated as the superposition of 4 rectangular dislocation models[71] associated with fault segments. The dislocations are vertical, with top at 50 m and bottom at 3000 m of depth. Since the PF mostly shows strike-slip and opening components, we considered only these components of the source mechanisms of the 4 dislocation models. For fixed model geometries, after computing the Green's functions for unit slip and opening, and for each model/segment, the relationship between predicted deformation and segment kinematics (i.e., strike-slips and openings) becomes linear. Thus, the strike-slip and opening parameters of the 4 segments can be simultaneously estimated from measurements by superimposing their contributions and inverting a linear system of equations. Since the system was overdetermined, we solved it in a least-squares sense. In order to suppress unrealistic scattered solutions and guarantee a consistency of contiguity, a spatial Laplacian constraint was introduced in the inverse problem formulation[72]. The Lagrange multiplier was obtained by the U-curve method[73].

Data availability

The seismic and GPS data are available from the INGV but restrictions apply to the availability of these data, which were used under license for the current study, and so are not publicly available. Data are however available from the authors upon reasonable request and with permission of the INGV (Salvatore Alparone, salvatore.alparone@ingv.it; Andrea Ursino, andrea.ursino@ingv.it). We provided an xls file as Supplementary Data. 1 with the features of all the detected repeating earthquake families of PF (https://doi.org/10.5281/zenodo.4727613). This file contains: a first sheet with the main features of all the families; a sheet per each family with information about all the earthquakes composing the family, as well as figures with waveforms and cross-correlation matrices.

Code availability

Codes used in this study are available from the authors upon request. Matlab version 2020a was used to generate all the figures.

Received: 2 December 2020; Accepted: 30 April 2021;

References

1. Tsujiura, M. Characteristic frequencies for earthquake families and their tectonic implications: Evidence from earthquake swarms in the Kanto district, Japan. *Pure Appl. Geophys.* **121**, 573–600 (1983).
2. Schaff, D. P. & Beroza, G. C. Coseismic and postseismic velocity changes measured by repeating earthquakes. *J. Geophys. Res. Solid Earth* **109**, https://doi.org/10.1029/2004JB003011 (2004).
3. Uchida, N. & Bürgmann, R. Repeating earthquakes. *Annu. Rev. Earth Planet. Sci.* **47**, 305–332 (2019).
4. Nadeau, R. M. & McEvilly, T. V. Fault slip rates at depth from recurrence intervals of repeating microearthquakes. *Science* **285**, 718–721 (1999).
5. Nadeau, R. M. & McEvilly, T. V. Periodic pulsing of characteristic microearthquakes on the San Andreas fault. *Science* **303**, 220–222 (2004).
6. Uchida, N. Detection of repeating earthquakes and their application in characterizing slow fault slip. *Prog. Earth Planet. Sci.* **6**, 40 (2019).
7. Yamashita, Y., Shimizu, H. & Goto, K. Small repeating earthquake activity, interplate quasi-static slip, and interplate coupling in the Hyuga-nada, southwestern Japan subduction zone. *Geophys. Res. Lett.* **39**, 1–5 (2012).
8. Hotovec-Ellis, A. J., Vidale, J. E., Gomberg, J., Thelen, W. & Moran, S. C. Changes in seismic velocity during the first 14 months of the 2004-2008 eruption of Mount St. Helens, Washington. *J. Geophys. Res. Solid Earth* **120**, 6226–6240 (2015).
9. Thelen, W., Malone, S. D. & West, M. Multiplets. Their behavior and utility at dacitic and andesitic volcanic centers. *J. Geophys. Res. Solid Earth* **116**, https://doi.org/10.1029/2010JB007924 (2011).
10. Allstadt, K. & Malone, S. D. Swarms of repeating stick-slip icequakes triggered by snow loading at Mount Rainier volcano. *J. Geophys. Res. Earth Surf.* **119**, 1180–1203 (2014).
11. Helmstetter, A., Nicolas, B., Comon, P. & Gay, M. Basal icequakes recorded beneath an alpine glacier (Glacier d'Argentière, Mont Blanc, France): Evidence for stick-slip motion? *J. Geophys. Res. Earth Surf.* **120**, 379–401 (2015).
12. Taira, T., Silver, P. G., Niu, F. & Nadeau, R. M. Remote triggering of fault-strength changes on the San Andreas fault at Parkfield. *Nature* **461**, 636–639 (2009).
13. Cannata, A. Crustal changes at Mt. Etna volcano accompanying the 2002-2003 eruption as inferred from a repeating earthquake analysis. *Geophys. Res. Lett.* **39**, 2–7 (2012).
14. Brancato, A. & Gresta, S. High precision relocation of microearthquakes at Mt. Etna (1991-1993 eruption onset): A tool for better understanding the volcano seismicity. *J. Volcanol. Geotherm. Res.* **124**, 219–239 (2003).
15. Musumeci, C. et al. Foreland seismicity associated with strike-slip faulting in southeastern Sicily, Italy: seismotectonic implications and seismic hazard assessment. *Phys. Earth Planet. Inter.* **307**, 106553 (2020).
16. Kimura, H., Kasahara, K., Igarashi, T. & Hirata, N. Repeating earthquake activities associated with the Philippine Sea plate subduction in the Kanto district, central Japan: A new plate configuration revealed by interplate aseismic slips. *Tectonophysics* **417**, 101–118 (2006).
17. Waldhauser, F., Ellsworth, W. L., Schaff, D. P. & Cole, A. Streaks, multiplets, and holes: High-resolution spatio-temporal behavior of Parkfield seismicity. *Geophys. Res. Lett.* **31**, 2–5 (2004).
18. Dominguez, L. A., Taira, T. & Santoyo, M. A. Spatiotemporal variations of characteristic repeating earthquake sequences along the Middle America Trench in Mexico. *J. Geophys. Res. Solid Earth* **121**, 8855–8870 (2016).
19. Kim, A., Dreger, D. S., Taira, T. & Nadeau, R. M. Changes in repeating earthquake slip behavior following the 2004 Parkfield main shock from waveform empirical Green's functions finite-source inversion. *J. Geophys. Res. Solid Earth* **121**, 1910–1926 (2016).
20. Cannata, A. et al. Long period and very long period events at Mt. Etna volcano: characteristics, variability and causality, and implications for their sources. *J. Volcanol. Geotherm. Res.* **187**, 227–249 (2009).
21. Cannata, A., Alparone, S. & Ursino, A. Repeating volcano-tectonic earthquakes at Mt. Etna volcano (Sicily, Italy) during 1999-2009. *Gondwana Res.* **24**, 1223–1236 (2013).
22. Patanè, D., Cocina, O., Falsaperla, S., Privitera, E. & Spampinato, S. Mt. Etna volcano: a seismological framework. in *Geophysical Monograph Series,* Vol., 143, 147–165 (Blackwell Publishing Ltd, 2004).
23. Alparone, S. et al. Instrumental seismic catalogue of Mt. Etna earthquakes (Sicily, Italy): Ten years (2000-2010) of instrumental recordings. *Ann. Geophys.* **58**, S0435 (2015).
24. Alparone, S. & Gambino, S. High precision locations of multiplets on south-eastern flank of Mt. Etna (Italy): reconstruction of fault plane geometry. *Phys. Earth Planet. Inter.* **135**, 281–289 (2003).
25. Lentini, F. The geology of the Mt. Etna basement. *Mem. Soc. Geol. It.* **23**, 7–25 (1982).
26. Monaco, C., De Guidi, G. & Ferlito, C. The Morphotectonic map of Mt. Etna. *Ital. J. Geosci.* **129**, 408–428 (2010).
27. Urlaub, M. et al. Gravitational collapse of Mount Etna's southeastern flank. *Sci. Adv* **4**, http://advances.sciencemag.org/ (2018).
28. Palano, M. et al. Kinematics and strain analyses of the eastern segment of the Pernicana Fault (Mt. Etna, Italy) derived from geodetic techniques (1997-2005). *Ann. Geophys.* **49**, 1105–1117 (2006).
29. Azzaro, R., Branca, S., Gwinner, K. & Coltelli, M. The volcano-tectonic map of Etna volcano, 1:100.000 scale: an integrated approach based on a morphotectonic analysis from high-resolution DEM constrained by geologic, active faulting and seismotectonic data. *Ital. J. Geosci.* **131**, 153–170 (2012).
30. Bonforte, A., Bonaccorso, A., Guglielmino, F., Palano, M. & Puglisi, G. Feeding system and magma storage beneath Mt. Etna as revealed by recent inflation/deflation cycles. *J. Geophys. Res. Solid Earth* **113**, https://doi.org/10.1029/2007JB005334 (2008).
31. Gresta, S., Ghisetti, F., Privitera, E. & Bonanno, A. Coupling of eruptions and earthquakes at Mt. Etna (Sicily, Italy): a case study from the 1981 and 2001 events. *Geophys. Res. Lett.* **32**, 1–4 (2005).
32. Borgia, A., Ferrari, L. & Pasquarè, G. Importance of gravitational spreading in the tectonic and volcanic evolution of Mount Etna. *Nature* **357**, 231–235 (1992).
33. Acocella, V., Behncke, B., Neri, M. & D'Amico, S. Link between major flank slip and 2002-2003 eruption at Mt. Etna (Italy). *Geophys. Res. Lett.* **30**, 10–13 (2003).
34. Neri, M., Acocella, V. & Behncke, B. The role of the Pernicana Fault System in the spreading of Mt. Etna (Italy) during the 2002-2003 eruption. *Bull. Volcanol.* **66**, 417–430 (2004).
35. Lanzafame, G. et al. Structural features of the July-August 2001 Mount Etna eruption: evidence for a complex magma supply system. *J. Geol. Soc. London.* **160**, 531–544 (2003).
36. Ruch, J. et al. Seismo-tectonic behavior of the Pernicana Fault System (Mt Etna): a gauge for volcano flank instability? *J. Geophys. Res. Solid Earth* **118**, 4398–4409 (2013).
37. Distefano, G., Gresta, S. & Longo, V. Caratteri della sismicità del versante nord-orientale dell'Etna. *Proc. 9° Nation. Conf. GNGTS* 253–260 (1990).
38. Alparone, S. et al. Seismological features of the Pernicana-Provenzana Fault System (Mt. Etna, Italy) and implications for the dynamics of northeastern flank of the volcano. *J. Volcanol. Geotherm. Res.* **251**, 16–26 (2013).
39. Alparone, S., Carletti, A., Ferrucci, F., Gresta, S. & Latini, G. Studio di microterremoti lungo una asperità all'Etna. *Proc. 11° Nation. Conf. GNGTS* 163-170 (1992).
40. Bonforte, A., Branca, S. & Palano, M. Geometric and kinematic variations along the active Pernicana fault: Implication for the dynamics of Mount Etna NE flank (Italy). *J. Volcanol. Geotherm. Res.* **160**, 210–222 (2007).
41. Igarashi, T., Matsuzawa, T. & Hasegawa, A. Repeating earthquakes and interplate aseismic slip in the northeastern Japan subduction zone. *J. Geophys. Res. Solid Earth* **108**, 1–9 (2003).
42. Nadeau, R. M. & Johnson, L. R. Seismological studies at Parkfield VI: moment release rates and estimates of source parameters for small repeating earthquakes. *Bull. Seismol. Soc. Am.* **88**, 790–814 (1998).
43. Azzaro, R. et al. New evidence for the form and extent of the Pernicana fault system (Mt. Etna) from structural and soil-gas surveying. *J. Volcanol. Geotherm. Res.* **84**, 143–152 (1998).
44. Tibaldi, A. & Groppelli, G. Volcano-tectonic activity along structures of the unstable NE flank of Mt. Etna (Italy) and their possible origin. *J. Volcanol. Geotherm. Res.* **115**, 277–302 (2002).
45. D'Amato, D. et al. Holocene slip rate variability along the Pernicana fault system (Mt. Etna, Italy): evidence from offset lava flows. *Bull. Geol. Soc. Am.* **129**, 304–317 (2017).
46. Aloisi, M., Jin, S., Pulvirenti, F. & Scaltrito, A. The December 2015 Mount Etna eruption: an analysis of inflation/deflation phases and faulting processes. *J. Geodyn.* **107**, 34–45 (2017).

47. Currenti, G. et al. Modeling of ALOS and COSMO-SkyMed satellite data at Mt Etna: Implications on relation between seismic activation of the Pernicana fault system and volcanic unrest. *Remote Sens. Environ.* **125**, 64–72 (2012).
48. Yu, W. C. Shallow-focus repeating earthquakes in the Tonga-Kermadec-Vanuatu subduction zones. *Bull. Seismol. Soc. Am.* **103**, 463–486 (2013).
49. Chen, K. H., Bürgmann, R. & Nadeau, R. M. Do earthquakes talk to each other? Triggering and interaction of repeating sequences at Parkfield. *J. Geophys. Res. Solid Earth* **118**, 165–182 (2013).
50. Harris, R. A. Introduction to special section: stress triggers, stress shadows, and implications for seismic hazard. *J. Geophys. Res. Solid Earth* **103**, 24347–24358 (1998).
51. Hill, D. P. et al. Seismicity remotely triggered by the magnitude 7.3 landers, California, earthquake. *Science* **260**, 1617–1623 (1993).
52. Alparone, S. C. et al Mt. Etna Revised and Concise Seismic Catalog from 1999 (EtnaRCSC) [Data set]. *Ist. Naz. di Geofis. e Vulcanol. (INGV).* https://doi.org/10.13127/ETNASC/ETNARCSC (2020).
53. Alparone, S. C. et al. Mt. Etna Seismic Catalog 2011-2013 (Version 1) [Data set]. *Ist. Naz. di Geofis. e Vulcanol.* https://doi.org/10.13127/ETNASC/2011_2013 (2020).
54. Alparone, S. C. et al. Mt. Etna Seismic Catalog 2014-2016 (Version 1) [Data set]. *Ist. Naz. di Geofis. e Vulcanol.* https://doi.org/10.13127/ETNASC/2014_2016 (2020).
55. Lahr, J. C. HYPOELLIPSE/VERSION 2.0: a computer program for determining local earthquake hypocentral parameters, magnitude and first motion pattern. *U.S. Geol. Surv., Open-File* **512**, 81 (1989).
56. Hirn, A., Nercessian, A., Sapin, M., Ferrucci, F. & Wittlinger, G. Seismic heterogeneity of Mt Etna: structure and activity. *Geophys. J. Int.* **105**, 139–153 (1991).
57. Patane, D., Ferrucci, F. & Gresta, S. Spectral features of microearthquakes in volcanic areas: attenuation in the crust and amplitude response of the site at Mt. Etna, Italy. *Bull. Seismol. Soc. Am.* **84**, 1842–1860 (1994).
58. Richter, C. F. *Elementary Seismology*. (W. H. Freeman and Co., 1958).
59. Green, D. N. & Neuberg, J. Waveform classification of volcanic low-frequency earthquake swarms and its implication at Soufrière Hills Volcano, Montserrat. *J. Volcanol. Geotherm. Res.* **153**, 51–63 (2006).
60. Barani, S., Ferretti, G., Massa, M. & Spallarossa, D. The waveform similarity approach to identify dependent events in instrumental seismic catalogues. *Geophys. J. Int.* **168**, 100–108 (2007).
61. Barreca, G., Bonforte, A. & Neri, M. A pilot GIS database of active faults of Mt. Etna (Sicily): a tool for integrated hazard evaluation. *J. Volcanol. Geotherm. Res.* **251**, 170–186 (2013).
62. Azzaro, R., Mattia, M. & Puglisi, G. Fault creep and kinematics of the eastern segment of the Pernicana Fault (Mt. Etna, Italy) derived from geodetic observations and their tectonic significance. *Tectonophysics* **333**, 401–415 (2001).
63. Chen, K. H., Nadeau, R. M. & Rau, R. J. Characteristic repeating earthquakes in an arc-continent collision boundary zone: the Chihshang fault of eastern Taiwan. *Earth Planet. Sci. Lett.* **276**, 262–272 (2008).
64. Uchida, N., Matsuzawa, T., Hasegawa, A. & Igarashi, T. Interplate quasi-static slip off Sanriku, NE Japan, estimated from repeating earthquakes. *Geophys. Res. Lett.* **30**, 1–4 (2003).
65. Giampiccolo, E., D'Amico, S., Patanè, D. & Gresta, S. Attenuation and source parameters of shallow microearthquakes at Mt. Etna Volcano, Italy. *Bull. Seismol. Soc. Am.* **97**, 184–197 (2007).
66. Palano, M. et al. Etn@ref: A geodetic reference frame for Mt. Etna GPS networks. *Ann. Geophys.* **53**, 49–57 (2010).
67. Bonforte, A. et al. Global positioning system survey data for active seismic and volcanic areas of eastern Sicily, 1994 to 2013. *Sci. Data* **3**, 1–13 (2016).
68. Guglielmino, F. et al. Analysis of satellite and in situ ground deformation data integrated by the SISTEM approach: the April 3, 2010 earthquake along the Pernicana fault (Mt. Etna - Italy) case study. *Earth Planet. Sci. Lett.* **312**, 327–336 (2011).
69. Bonforte, A. et al. Soil gases and SAR measurements reveal hidden faults on the sliding flank of Mt. Etna (Italy). *J. Volcanol. Geotherm. Res.* **251**, 27–40 (2013).
70. Herring, T. A., King, R. W. & McClusky, S. C. Introduction to GAMIT/GLOBK, Release 10. 4 (2010).
71. Okada, B. Surface deformation due to shear and tensile faults in a half-space. *Bull. Seismol. Soc. Am.* **75**, 1135–1154 (1985).
72. Jónsson, S., Zebker, H., Segall, P. & Amelung, F. Fault slip distribution of the 1999 Mw 7.1 Hector Mine, California, earthquake, estimated from satellite radar and GPS measurements. *Bull. Seismol. Soc. Am.* **92**, 1377–1389 (2002).
73. Wang, L., Zhao, X. & Gao, H. A method for determining the regularization parameter and the relative weight ratio of the seismic slip distribution with multi-source data. *J. Geodyn.* **118**, 1–10 (2018).
74. Tarquini, S., Isola, I., Favalli, M. & Battistini, A. TINITALY, a digital elevation model of Italy with a 10 m-cell size (Version 1.0) [Data set]. *Ist. Naz. di Geofis. e Vulcanol. (INGV).* https://doi.org/10.13127/TINITALY/1.0 (2007).
75. Lentini, F., Carbone, S. & Guarnieri, P. Collisional and Postcollisional Tectonics of the Apenninic-Maghrebian Orogen (Southern Italy). In *Postcollisional Tectonics and Magmatism in the Mediterranean Region and Asia* Vol. 409, 57–81 (Geological Society of America, 2006).

Acknowledgements

We are indebted to the technicians of the INGV, Osservatorio Etneo for enabling the acquisition of seismic and ground deformation data. Thanks also go to Stephen Conway for revising the English form of the manuscript. This work was funded by CHANCE project, II Edition, Università degli Studi di Catania (principal investigator A. Cannata) and grant PIACERI, 2020–22 programme (PAROSSISMA project, code 22722132140; principal investigator Marco Viccaro). We thank Maurizio Battaglia for helpful comments on the manuscript. We also thank two anonymous reviewers for their suggestions that greatly helped to improve the paper.

Author contributions

A.C., S.G., and A.I. designed the study. A.C. and A.I. analyzed the repeating earthquakes data. F.C. and A.B. analyzed the GPS ground deformation data. S.A., A.C., S.G., A.I., and A.U. analyzed the general seismicity data. S.A., A.B., A.C., F.C., S.C., S.G., A.I., E.R., and A.U. wrote the manuscript and contributed to the interpretation of results.

Competing interests

The authors declare no competing interests.

Additional information

Supplementary information The online version contains supplementary material available at https://doi.org/10.1038/s43247-021-00188-6.

Correspondence and requests for materials should be addressed to A.C. or A.I.

Peer review information *Communications Earth & Environment* thanks the anonymous reviewers for their contribution to the peer review of this work. Primary handling editor: Joe Aslin.

Reprints and permission information is available at http://www.nature.com/reprints